28. Materials and methods are available as supporting material on *Science* Online.
29. Y. Zhang, H. Li, *Acta Crystallogr D. Biol. Crystallogr.* **60**, 447 (2004).
30. H. Li, J. Abelson, *J. Mol. Biol.* **302**, 639 (2000).
31. J. L. Diener, P. B. Moore, *Mol. Cell* **1**, 883 (1998).
32. C. Biot, E. Buisine, J. M. Kwasigroch, R. Wintjens, M. Rooman, *J. Biol. Chem.* **277**, 40816 (2002).
33. E. Hershkovitz *et al.*, *Nucleic Acids Res.* **31**, 6249 (2003).
34. P. Nissen, J. A. Ippolito, N. Ban, P. B. Moore, T. A. Steitz, *Proc. Natl. Acad. Sci. U.S.A.* **98**, 4899 (2001).
35. D. J. Battle, J. A. Doudna, *Proc. Natl. Acad. Sci. U.S.A.* **99**, 11676 (2002).
36. C. R. Trotta, S. V. Paushkin, M. Patel, H. Li, S. W. Peltz, *Nature* (in press).
37. F. Miao, J. Abelson, *J. Biol. Chem.* **268**, 672 (1993).

38. We thank J. Abelson, C. Chapman, B. Miller, C. Trotta, W. Yang (FSU), and W. Yang (NIH) for inspiring discussions and for critical reading of the manuscript and R. Dhanarajan for assistance in cloning. This work was funded, in part, by grants from Florida Biomedical Research (BM002 to H.L.), American Heart Association Florida/Puerto Rico Affiliate (030396B to H.L.), and National Science Foundation (MCB-0517300 to H.L). K.C. is an American Heart Association Florida/Puerto Rico Affiliate predoctoral fellow (0415091B). X-ray diffraction data were collected at both the Northeastern Collaborative Access Team (NE-CAT) BM-8 beamline and the Southeast Regional Collaborative Access Team (SER-CAT) 22-ID beamline at the Advanced Photon Source, Argonne National Laboratory. Supporting institutions may be found at http://necat.chem.cornell.edu/ and www.ser-cat.org/members.html. Use of the Advanced Photon Source was supported by the U.S. Department of Energy, Office of Science, Office of Basic Energy Sciences, under Contract No. W-31-109-Eng-38. Coordinates and structure factors have been deposited in the Protein Data Bank (PDB) with accession number 2GJW.

Supporting Online Material

www.sciencemag.org/cgi/content/full/312/5775/906/DC1
Materials and Methods
Figs. S1 to S5
Table S1
References

23 February 2006; accepted 5 April 2006
10.1126/science.1126629

Molecular Sorting by Electrical Steering of Microtubules in Kinesin-Coated Channels

Martin G. L. van den Heuvel, Martijn P. de Graaff, Cees Dekker*

Integration of biomolecular motors in nanoengineered structures raises the intriguing possibility of manipulating materials on nanometer scales. We have managed to integrate kinesin motor proteins in closed submicron channels and to realize active electrical control of the direction of individual kinesin-propelled microtubule filaments at Y junctions. Using this technique, we demonstrate molecular sorting of differently labeled microtubules. We attribute the steering of microtubules to electric field–induced bending of the leading tip. From measurements of the orientation-dependent electrophoretic motion of individual, freely suspended microtubules, we estimate the net applied force on the tip to be in the picoNewton range and we infer an effective charge of 12 e^- per tubulin dimer under physiological conditions.

Recent years have witnessed a strong interest in the exploration of biomolecular motors in nanotechnology (*1*–*4*). A molecular motor such as kinesin, which translocates in 8-nm steps along microtubule filaments through hydrolysis of adenosine triphosphate (ATP) (*5*), can potentially be used as the workhorse in miniaturized analytical systems or nanoelectromechanical systems (*6*, *7*). In particular, it is envisioned that microtubule shuttles translocating over kinesin-coated tracks can be used to carry a specific cargo to designated places on a chip (*8*). First steps toward such applications have been realized, such as partial confinement of microtubules to micron-sized kinesin-coated trenches (*9*–*11*), docking of shuttles to their tracks (*12*), rectification of motility (*13*, *14*), and coupling of cargo (*15*). The much-sought-after goal of dynamic control of the direction of individual microtubules, a key requirement for molecular sorting applications, has not been achieved so far. Attempts to use electric fields to manipulate the negatively charged microtubules have only resulted in large-scale alignment (*16*) or bulk transport of the filaments (*11*, *12*).

In this report, we reconstituted the kinesin-microtubule transport system in enclosed fluidic channels, which represents two major advances. First, fluidic channels achieved full confinement of the microtubules to their tracks, without the need for any surface modifications or selective patterning of kinesin molecules in open-trench structures. Second, the confined geometry of channels allowed the localized application of strong, directed electric fields, which could be exploited to steer individual microtubules, as well as to perform single-molecule biophysical experiments. By measuring the electrophoretic motion of individual microtubules, we determined the magnitude of the electric field–induced force on the microtubule tip, and we directly confirmed the predicted anisotropy in electrophoretic mobility.

We fabricated fluidic channels 800 nm deep (*17*) between entrance holes in fused-silica substrates and sealed them (Fig. 1, A and B). Microtubule motility was reconstituted in the channels by a pressure-driven flow to flush the necessary protein constituents (casein, kinesin, and fluorescently labeled paclitaxel-stabilized associated protein–free microtubules) from the entrance reservoirs into the channels (Fig. 1C). Using epifluorescence microscopy, we could discern microtubules moving on either the top or bottom surface of a channel by adjusting the focus of the objective (Fig. 1D). The enclosed geometry of the device completely confined the microtubules to their tracks (Fig. 1E). All regions could be coated with kinesin proteins, even less accessible regions in more complicated networks, such as bends (Fig. 1F). The speed of the microtubules in our channels (0.75 ± 0.02 μm/s) was the same as on a glass coverslip in a standard flow cell (0.74 ± 0.04 μm/s). By applying a voltage difference between platinum electrodes inserted in reservoirs at either end of a perpendicular cross-channel, we induced an electric field **E** perpendicular to the direction of microtubule motion (Fig. 2A). In this way, the electrical force on the negatively charged microtubules was directed opposite to the electric field.

We demonstrated that microtubules can be directed with an electric field. The trajectory of a microtubule that was subjected to an electric field of strength $|\mathbf{E}|$ = 35 kV/m (70 V over 2 mm) is shown in Fig. 2B. At the beginning of the path, the microtubule was oriented perpendicular to the electric field. As the microtubule progressed, its leading end gradually oriented itself opposite to the applied field, until the microtubule finally changed course by 90° and moved parallel to the electric field and toward the positive electrode. A trace of the leading- and trailing-end coordinates of the microtubule showed that they followed exactly the same path (Fig. 2B). This clearly indicates that there was no motion of the microtubule perpendicular to its long axis, which is expected if kinesin molecules hold onto the microtubule. Up to 110 kV/m, we did not observe a measurable increase or decrease of the microtubule velocity due to the electric field (*18*).

The electric force was used to actively steer individual microtubules into a desired channel of a Y junction, across and through which a perpendicular channel was fabricated in order to confine the electric field. As a microtubule approached the junction, it was steered into the right channel by adjustment of the perpendicular electric field, whose magnitude was between 0

Kavli Institute of Nanoscience, Section Molecular Biophysics, Delft University of Technology, Lorentzweg 1, 2628 CJ Delft, Netherlands.

*To whom correspondence should be addressed. E-mail: dekker@mb.tn.tudelft.nl

equilibrium position toward the direction of higher potential and thereby increases the probability of finding the next binding site in this direction.

The field-dependent trajectories of microtubules were traced to quantify the microscopic bending in experiments analogous to Fig. 2B. For $|\mathbf{E}| = 0$, the average path of several ($N = 18$) microtubules was indeed a straight line in the initial direction of motion (Fig. 2F). For $|\mathbf{E}| = 35$ kV/m, the average microtubule path deviated from the straight path, ultimately orienting itself along the electric field ($N = 17$). The curvature of the trajectory upon entering the electric field was fitted by a circle of radius $R = 15 \pm 2$ μm. At a higher $|\mathbf{E}| = 70$ kV/m, the average bending of the path ($N = 10$) was more pronounced, and the curvature was described by a circle of $R = 8 \pm 1$ μm. The observed curvature of the microtubule path increased linearly with applied electric field (Fig. 2F, inset). The average bending radius did not depend on microtubule length.

The forces that act on the microtubules in the presence of an electric field have a nontrivial origin. The net force per unit length on the microtubule, f_{net}, stems from two components. First, the electric force was shown to equal the drag that moving counterions in the microtubule's double layer experience from the surrounding fluid: $f_e = c\mu_e\mathbf{E}$ (*20*–*22*). Here, c is the Stokes drag coefficient per unit length and μ_e the (negative) electrophoretic mobility of the microtubule. The second contribution to the force on the microtubule results from the fluid motion in the channel due to the field-driven motion of counterions at the glass channel walls. This electro-osmotic flow (EOF) (Fig. 2A) exerts a drag force on the microtubule opposite from the electric force, $f_{EOF} = c\mu_{EOF}\mathbf{E}$. Here, μ_{EOF} is the (positive) electro-osmotic mobility. At the beginning of the microtubule path, the electric field is perpendicular to the microtubule, resulting in a net force:

$$f_{net} = c_\perp(\mu_{e,\perp} + \mu_{EOF})\mathbf{E} \qquad (1)$$

Electrokinetic measurements were performed on single microtubules in order to measure the magnitude of this force. The electrophoretic mobility of rodlike polymers, such as microtubules, has only been treated theoretically, and is predicted to be anisotropic for perpendicular ($\mu_{e,\perp}$) and parallel ($\mu_{e,\parallel}$) orientations of the rod to the electric field (*20*, *23*):

$$\mu_{e,\parallel} = \frac{\varepsilon\zeta}{\eta} \text{ and } \mu_{e,\perp} = {}^2\!/_3 g_\perp \frac{\varepsilon\zeta}{\eta} \qquad (2)$$

Here, η and ε are the viscosity and dielectric constant of the fluid, respectively, and ζ is the electrostatic potential at the no-slip plane of the microtubule. The anisotropy factor $g_\perp$ accounts for the perturbation of the ionic atmosphere around the rod (*20*, *23*) and approaches a maximum value of $^3\!/_2$ for infinitely small Debye lengths (*24*). Measurements of these anisotropic electrophoretic mobilities of colloidal cylinders have not, as far as we know, been reported. The small height of our channels allowed us to observe individual microtubules in a single focal plane, which enabled us to test the predicted anisotropy of the mobility. The anisotropic mobilities induced an observable orientation-dependent velocity of microtubules, with components perpendicular (v_x) and parallel (v_y) to the electric field (fig. S1):

$$v_x = {}^1\!/_2(\mu_{e,\parallel} - \mu_{e,\perp})\sin 2\theta\cdot\mathbf{E}$$
$$v_y = [(\mu_{e,\parallel} - \mu_{e,\perp})\sin^2\theta + (\mu_{e,\perp} + \mu_{EOF})]\mathbf{E} \qquad (3)$$

Here, θ is the orientation of the filament with respect to the x axis (Fig. 3A). Note that the velocity is not necessarily collinear with the electric field. The EOF adds linearly as an orientation-independent velocity decrease in the y direction.

The electrophoretic motion of individual microtubules in channels without kinesin is shown in Fig. 3A. In accordance with the bending experiments, we observed that freely suspended microtubules move opposite to the applied electric field along the channel. Values of orientation-dependent v_x (Fig. 3B) and v_y (Fig. 3C) were measured for different $\mathbf{E}$. The red lines are fits of Eq. 3 through the binned data and clearly describe the θ dependence of the velocities very well. These data are direct evidence of the anisotropic electrophoretic microtubule mobility, and the amplitudes of the curves provide a straightforward measure of the anisotropy. As expected from Eq. 2, microtubules move fastest if they are oriented parallel to the

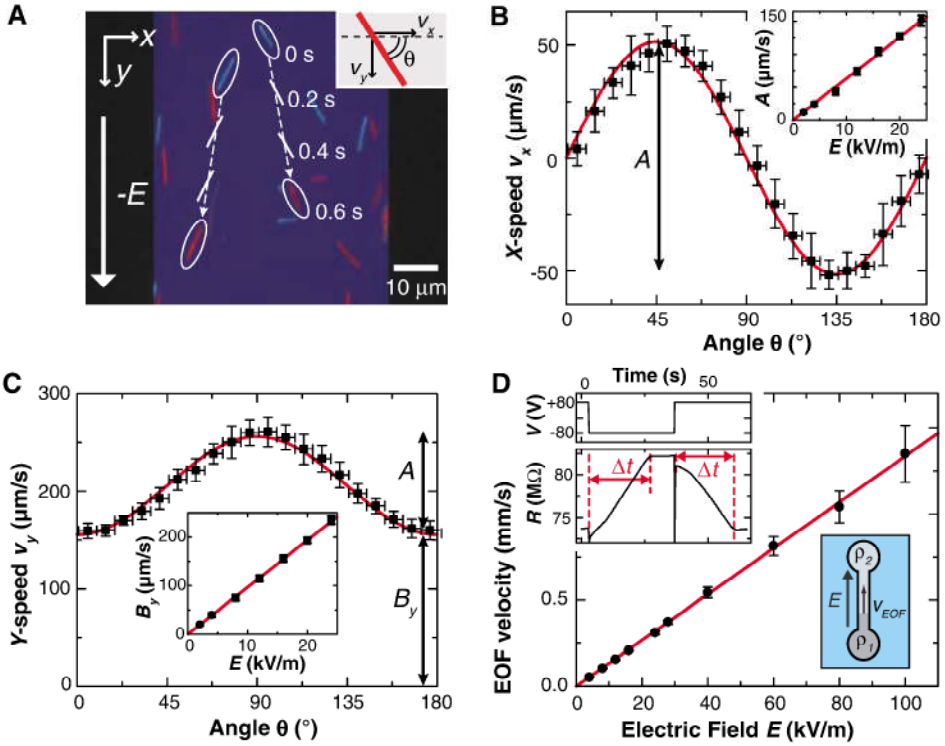

Fig. 3. Electrophoresis of single microtubules and measurement of the EOF velocity. All measurements were performed at neutral pH in the presence of 160 mM K^+. **(A)** Electrophoresis in channels of individual microtubules. Shown is an overlay of images at 0 s (blue microtubules) and at 0.6 s (red microtubules). Intermediate positions of two selected microtubules are indicated by white lines. The selected microtubules not only move in the direction of the electric field, but also perpendicular to it. **(B and C)** Binned data ($N = 1496$) of orientation-dependent electrophoretic velocities of microtubules in the x direction [perpendicular to the electric field (B)] and in the y direction [parallel to the electric field (C)]. Error bars denote standard deviation of binned data. The amplitudes A in both curves equal $(\mu_{e,\parallel} - \mu_{e,\perp})\mathbf{E}$. The offset of the v_y graph, $B_y = (\mu_{e,\perp} + \mu_{EOF})\mathbf{E} \propto f_{net}$, applied during steering as in Fig. 2A. (Insets) Linear relation between B_y and $\mathbf{E}$. There was no significant dependence of the velocity on microtubule length. **(D)** EOF velocity as a function of electric field, measured by monitoring the change in resistance of a channel that is replenished by a solution of a different resistivity ρ by an EOF. (Inset) Two typical measurements of the time Δt that it takes the EOF to replace a channel volume (length 5 mm) at $|V| = 80$ V. Each data point in the main graph represents an average of 4 to 6 separate measurements. The slope of the graph equals μ_{EOF}.

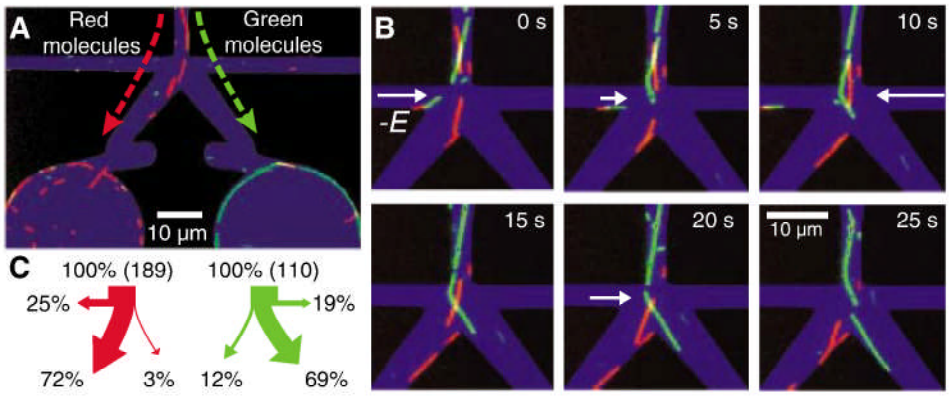

Fig. 4. Demonstration of molecular sorting. **(A)** Color image of a mixture of red- and green-labeled microtubules approaching a Y junction. Electrical force is used to steer microtubules carrying green and red fluorophores into the right and left reservoirs, respectively. **(B)** Example of successful sorting events for a green- and a red-labeled microtubule. As a function of time, first a green microtubule is steered into the right reservoir ($t \leq 10$ s), and subsequently a red microtubule is sent into the left reservoir. **(C)** Steering efficiencies for 189 red and 110 green microtubules. Steering of microtubules into the wrong reservoir (3 and 12%) was mainly due to differences in stiffness between microtubules or due to the simultaneous arrival of microtubules of opposite color. The fractions 19 and 25% of microtubules in the perpendicular channels are artificially high because microtubules were sometimes purposely directed into the perpendicular steering channel so as to avoid such errors.

electric field and slowest for perpendicular orientations (Fig. 3C). To extract the values of the anisotropic microtubule mobilities, we measured $\mu_{EOF} = (1.33 \pm 0.01) \times 10^{-8}$ m^{2}V^{-1}s^{-1} in our kinesin-coated channels (Fig. 3D), yielding $\mu_{e,\perp} = -(2.30 \pm 0.04) \times 10^{-8}$ m^{2}V^{-1}s^{-1} and $\mu_{e,\parallel} = -(2.93 \pm 0.02) \times 10^{-8}$ m^{2}V^{-1}s^{-1}. The anisotropy in electrophoretic mobility is not related to the well-known factor 2 anisotropy in Stokes drag coefficients (*25*), because, in electrophoresis, the retarding shear acts on the length scale of the Debye length λ_D, whereas, in Stokes drag, this length scale is on the order of the size of the object. The values of μ_{EOF}, $\mu_{e,\perp}$, and $\mu_{e,\parallel}$ are all constant over the probed range of electric fields (insets of Fig. 3, B to D).

These mobility measurements permit a calculation of the net force applied in the bending experiments (Eq. 1). From the values $c_\perp = (7.4 \pm 2.0) \times 10^{-3}$ kg/ms (*26*) and $(\mu_{e,\perp} + \mu_{EOF}) = -(9.7 \pm 0.2) \times 10^{-9}$ m^{2}V^{-1}s^{-1}, we calculated the net electrokinetic applied force on the microtubule as $f_{net} = [-(7.2 \pm 2.0) \times 10^{-11}$ N/V$]$ **E**. The forces applied in the bending experiments (Fig. 2F) thus ranged up to 5.0 ± 1.4 pN/μm at $|\mathbf{E}| = 70$ kV/m. Knowledge of the magnitude of this force allowed determination of both the persistence length and the surface charge of the microtubules.

The persistence length of the microtubule was determined from observations of the bending radius under a known perpendicular force. The bending of the microtubule tip can be expressed in terms of the free tip length δ [inversely proportional to motor density (*19*)] and its persistence length L_p. For perpendicular forces f_{net}, the induced curvature r^{-1} of the free tip, in the limit of small deflections, is as follows (Fig. 2E and fig. S2):

$$r^{-1} = \frac{1}{4k_BT}\frac{\delta^2}{L_p}f_{net} \qquad (4)$$

where k_B is Boltzmann's constant and T is temperature. We assert that the microscopic tip curvature r^{-1} equals the macroscopic path curvature R^{-1}. From the linear relation of R^{-1} versus f_{net} (Fig. 2F, inset, and Eq. 4), we determined $\delta^2/L_p = 0.41 \pm 0.12$ nm. We estimated $\delta = 0.26 \pm 0.06$ μm for the free tip length from our observations of the length of the shortest microtubules (0.52 ± 0.13 μm) that still moved in smooth trajectories in our channels. The persistence length of the microtubule's free tip was thus determined to be $L_p = 0.16 \pm 0.09$ mm. This value is on the low end of published values on paclitaxel-stabilized microtubules that find $L_p = 0.2$ to 5.2 mm (*27*, *28*), but the persistence length of the tip does not necessarily represent the persistence length of the entire microtubule (*29*).

The electric charge of a microtubule is determined in two independent ways from the electrophoretic mobilities. First, the value of $\mu_{e,\parallel}$ is proportional to ζ (Eq. 2), which is a direct measure of the surface charge density σ via the linear Grahame equation $\sigma = \varepsilon\zeta/\lambda_D$. From $\mu_{e,\parallel}$, we find that $\zeta = -37$ mV, which yields a surface charge density of 0.20 e$^-$/nm^2. A second measure of the surface charge follows from the value of $g_\perp$ (*20*, *23*). The experimentally determined anisotropy factor $g_\perp = {}^3/_2\,\mu_{e,\perp}/\mu_{e,\parallel} = 1.18$ yields a value of $\zeta = -50$ mV via the inverse transformation (*24*) $\zeta = \Im^{-1}(g_\perp, a/\lambda_D)$. This ζ corresponds to $\sigma = 0.27$ e$^-$/nm^2. The average of both measurements gives $\sigma = 0.24 \pm 0.04$ e$^-$/nm^2, with the error estimated from the difference between the two values (*30*).

From the measured σ and the known 25-nm diameter of a 13-protofilament microtubule, we calculated an effective charge of 12 ± 2 e$^-$ for the solution-exposed surface of the tubulin dimer. A rough estimate of the bare charge of the free dimer of 47 e$^-$ at pH = 6.9 follows from the crystal structure of the tubulin dimer (*31*), if one assumes the isolated dissociation constants of the individual amino acids. The effective charge constituted only about 25% of the bare charge, which can be attributed mainly to screening by counterions that are tightly bound to the microtubule surface.

Having developed an understanding of the steering mechanism of individual microtubules, we demonstrated the applicability of the electrical steering of microtubules in nanostructures by sorting a population of two different molecules on a chip (Fig. 4A, movie S1). To this end, we introduced a mixture of rhodamine- (red) and fluorescein-labeled (green) microtubules into our nanostructures. Using a color-sensitive camera, red microtubules approaching a Y junction were sent into the red-collecting reservoir and green microtubules into the green reservoir (Fig. 4B) by reversing the polarity of the electric field. After a series of successful single-molecule redirections, one reservoir contained predominantly red microtubules, whereas the other reservoir contained mainly green microtubules (Fig. 4A).

We quantified the sorting efficiency in Fig. 4C. A large fraction (72%) of the red microtubules approaching the junction were directed, as intended, into the red reservoir. Only 3% of the red microtubules incorrectly ended up in the green reservoir. The remainder of the red microtubules (25%) was steered into the perpendicular channel. A similar analysis was made for the green microtubules (69, 12, and 19%, respectively, Fig. 4C). The final result is that 91% of the microtubules sent into the left reservoir are red (136 out of 149), and 94% of the microtubules in the right reservoir are green (76 out of 81). Real use of this sorting method, e.g., for purification, will benefit from automation, which can be incorporated straightforwardly. The use of biomolecular motors for sorting forms an interesting alternative to existing pressure- or EOF-driven microfluidic devices (*32*–*34*) by which whole cells are sorted.

In conclusion, our experiments demonstrate the ability to electrically steer individual microtubules in enclosed submicron channels, as demonstrated by the single-molecule sorting of fluorescein- and rhodamine-labeled microtubules. The steering of microtubules is described in terms of force-induced bending of the free tip of the microtubule, which yields a persistence length $L_p = 0.16 \pm 0.09$ mm. Our single-microtubule electrophoresis experiments revealed an orientation-dependent electrophoretic

mobility and yield a charge of 12 ± 2 e$^-$ per tubulin dimer under physiological conditions. This value may be important to elucidate the effect of in vivo electric forces on microtubules. Endogenous physiological electric fields, with a typical value up to 10^3 V/m, are shown to be involved in cell division, wound healing (*35*), and embryonic cell development (*36*), but their microscopic effect has so far not been understood. The application of biomotors in nanofabricated environments is an exciting development, offering novel possibilities for future developments in lab-on-chip sorting or purification applications.

References and Notes

1. R. K. Soong *et al.*, *Science* **290**, 1555 (2000).
2. F. Patolsky, Y. Weizmann, I. Willner, *Nat. Mater.* **3**, 692 (2004).
3. J. Xi, J. J. Schmidt, C. D. Montemagno, *Nat. Mater.* **4**, 180 (2005).
4. H. Hess, V. Vogel, *J. Biotechnol.* **82**, 67 (2001).
5. M. J. Schnitzer, S. M. Block, *Nature* **388**, 386 (1997).
6. K. J. Bohm, J. Beeg, G. M. zu Horste, R. Stracke, E. Unger, *IEEE Trans. Adv. Packag.* **28**, 571 (2005).
7. R. Yokokawa *et al.*, *Nano Lett.* **4**, 2265 (2004).
8. H. Hess, G. D. Bachand, V. Vogel, *Chemistry* **10**, 2110 (2004).
9. J. Clemmens *et al.*, *Langmuir* **19**, 10967 (2003).
10. S. G. Moorjani, L. Jia, T. N. Jackson, W. O. Hancock, *Nano Lett.* **3**, 633 (2003).
11. L. Jia, S. G. Moorjani, T. N. Jackson, W. O. Hancock, *Biomed. Microdevices* **6**, 67 (2004).
12. M. G. L. van den Heuvel, C. T. Butcher, S. G. Lemay, S. Diez, C. Dekker, *Nano Lett.* **5**, 235 (2005).
13. Y. Hiratsuka, T. Tada, K. Oiwa, T. Kanayama, T. Q. P. Uyeda, *Biophys. J.* **81**, 1555 (2001).
14. M. G. L. van den Heuvel, C. T. Butcher, R. M. M. Smeets, S. Diez, C. Dekker, *Nano Lett.* **5**, 1117 (2005).
15. S. Ramachandran, K. Ernst, G. D. Bachand, V. Vogel, H. Hess, *Small* **2**, 330 (2006).
16. R. Stracke, K. J. Bohm, L. Wollweber, J. A. Tuszynski, E. Unger, *Biochem. Biophys. Res. Commun.* **293**, 602 (2002).
17. Materials and methods are available as supporting information on *Science* Online.
18. At large fields, higher than ~110 kV/m, we observed an effect on the microtubule velocity along the electric field. Microtubules moving parallel to the electric field displayed higher and lower speeds depending on the direction of the field. For fields oriented perpendicular to the long axis, microtubules displayed sideward motion. We are investigating these effects.
19. T. Duke, T. E. Holy, S. Leibler, *Phys. Rev. Lett.* **74**, 330 (1995).
20. D. Stigter, *J. Phys. Chem.* **82**, 1417 (1978).
21. D. Stigter, C. Bustamante, *Biophys. J.* **75**, 1197 (1998).
22. The electrophoretic force on stationary microtubules in the absence of a bulk EOF consists of a direct force on the negative microtubule charge, $-|\sigma|\mathbf{E}$, and an opposing indirect friction, τ, exerted by the microtubule's counterions moving along the electric field. The velocity of the counterions increases from 0 at the microtubule surface to $|\mu_e|\mathbf{E}$. If $\lambda_D \ll R$, the magnitude of $\tau = +|\sigma|\mathbf{E} - c|\mu_e|\mathbf{E}$ and also equals the total force density exerted on the double layer, plus the drag force exerted on the moving counterions (*21*).
23. D. Stigter, *Biopolymers* **31**, 169 (1991).
24. The value of $g_\perp$ only depends on the ζ potential of a microtubule and the relative thickness of the double layer (λ_D) with respect to the cylinder radius a, i.e., $g_\perp = \Im(\zeta, a/\lambda_D)$, and numerical values have been tabulated (*20*). In the limit of infinitely small λ_D, $g_\perp$ reaches its maximum value of 1.5 and $\mu_{e,\perp} \rightarrow \mu_{e,\mathrm{II}}$. The experimentally determined value of $g_\perp$ is thus a measure of the ζ potential by $\zeta = \Im^{-1}(g_\perp, a/\lambda_D)$, using $a = 12.5$ nm and $\lambda_D = 0.8$ nm for the Debye length in our 160 mM buffer.
25. A. J. Hunt, F. Gittes, J. Howard, *Biophys. J.* **67**, 766 (1994).
26. We calculate $c_\perp$ using the analytical result from Hunt *et al.* (*25*) with the following numerical values: Microtubule radius $a = 12.5 \pm 1$ nm, viscosity $\eta = 0.89 \pm 0.09 \times 10^{-3}$ kg/ms, and $h = 30 \pm 10$ nm for the distance of the microtubule axis to the surface.
27. F. Gittes, B. Mickey, J. Nettleton, J. Howard, *J. Cell Biol.* **120**, 923 (1993).
28. H. Felgner, R. Frank, M. Schliwa, *J. Cell Sci.* **109**, 509 (1996).
29. For long microtubules and high kinesin density, the persistence length of the microtubule trajectory L_{tr} equals the persistence length of the tip L_p (*19*). This trajectory persistence length of microtubules in the absence of electric fields has been quantified to be 0.11 mm (*37*). Our value of the tip persistence length is close to this value. The suggestion of Kis *et al.* (*38*) that protofilament sliding reduces the stiffness of short lengths of microtubules could serve as a possible explanation of the low L_p, together with possible defects in the tip structure.
30. The use of the linear Grahame equation is strictly speaking only valid for $\zeta \ll k_B T/e = 26$ mV. However, at $\zeta = 50$ mV, the use of the linearized Grahame equation introduces an error in σ of only 14%. The use of the nonlinear version of the Grahame would invoke an unknown source of error, because we would then have to assume a value for the double-layer capacitance of the microtubule.
31. E. Nogales, S. G. Wolf, K. H. Downing, *Nature* **393**, 191 (1998).
32. P. S. Dittrich, P. Schwille, *Anal. Chem.* **75**, 5767 (2003).
33. A. Y. Fu, C. Spence, A. Scherer, F. H. Arnold, S. R. Quake, *Nat. Biotechnol.* **17**, 1109 (1999).
34. H. A. Stone, A. D. Stroock, A. Ajdari, *Annu. Rev. Fluid Mech.* **36**, 381 (2004).
35. B. Song, M. Zhao, J. V. Forrester, C. D. McCaig, *Proc. Natl. Acad. Sci. U.S.A.* **99**, 13577 (2002).
36. K. R. Robinson, L. F. Jaffe, *Science* **187**, 70 (1975).
37. T. Nitta, H. Hess, *Nano Lett.* **5**, 1337 (2005).
38. A. Kis *et al.*, *Phys. Rev. Lett.* **89**, 248101 (2002).

39. We thank J. Howard and S. Diez for kindly providing us with the kinesin expression vector and for advice with protocols; S. G. Lemay, I. Dujovne, and D. Stein for useful discussions; Y. Garini and Olympus Netherlands for lending optical equipment; and Hamamatsu Germany for kindly providing us a C7780 color camera. This work was funded by the Dutch Organization for Scientific Research (NWO) and the European Community Biomach program.

Supporting Online Material

www.sciencemag.org/cgi/content/full/312/5775/910/DC1
Materials and Methods
SOM Text
Figs. S1 and S2
References and Notes
Movie S1

23 December 2005; accepted 9 March 2006
10.1126/science.1124258

PIN Proteins Perform a Rate-Limiting Function in Cellular Auxin Efflux

Jan Petrášek,[1,2] Jozef Mravec,[3] Rodolphe Bouchard,[4] Joshua J. Blakeslee,[5] Melinda Abas,[6] Daniela Seifertová,[1,2,3] Justyna Wiśniewska,[3,7] Zerihun Tadele,[8] Martin Kubeš,[1,2] Milada Čovanová,[1,2] Pankaj Dhonukshe,[3] Petr Skůpa,[1,2] Eva Benková,[3] Lucie Perry,[1] Pavel Křeček,[1,2] Ok Ran Lee,[5] Gerald R. Fink,[9] Markus Geisler,[4] Angus S. Murphy,[5] Christian Luschnig,[6] Eva Zažímalová,[1]* Jiří Friml[3,10]

Intercellular flow of the phytohormone auxin underpins multiple developmental processes in plants. Plant-specific pin-formed (PIN) proteins and several phosphoglycoprotein (PGP) transporters are crucial factors in auxin transport–related development, yet the molecular function of PINs remains unknown. Here, we show that PINs mediate auxin efflux from mammalian and yeast cells without needing additional plant-specific factors. Conditional gain-of-function alleles and quantitative measurements of auxin accumulation in *Arabidopsis* and tobacco cultured cells revealed that the action of PINs in auxin efflux is distinct from PGP, rate-limiting, specific to auxins, and sensitive to auxin transport inhibitors. This suggests a direct involvement of PINs in catalyzing cellular auxin efflux.

Auxin, a regulatory compound, plays a major role in the spatial and temporal coordination of plant development (*1*–*3*). The directional active cell-to-cell transport controls asymmetric auxin distribution, which underlies multiple patterning and differential growth processes (*4*–*7*). Genetic approaches in *Arabidopsis thaliana* identified candidate genes coding for regulators of auxin transport, among them permease-like AUX1 (*8*), plant-specific PIN proteins (*9*) (fig. S1), and homologs of human multiple drug resistance transporters PGP1 and PGP19 (*10*, *11*). PGP1 has been shown to mediate the efflux of auxin from *Arabidopsis* protoplasts and heterologous systems such as yeast and HeLa cells (*12*). Similarly, PIN2 in yeast conferred decreased retention of structural auxin analogs (*13*, *14*). Plants defective in PIN function show altered auxin distribution and diverse developmental defects, all of which can be phenocopied by chemical inhibition of auxin efflux (*1*, *4*–*7*, *9*). All results demonstrate that PINs are essential components of the auxin transport machinery, but the exact mechanism of their action remains unclear.

Studies of the molecular function of PINs have been hampered mainly by the technical inability to quantitatively assess auxin flow across the plasma membrane (PM) in a multicellular system. We therefore established *Arabidopsis* cell suspension culture from the *XVE-PIN1* line, in which we placed the *PIN1* sequence under control of the estradiol-inducible promoter (*15*). Treatment with estradiol led to the activation of *PIN1* expression as shown by the coexpressed green fluorescent protein (GFP) reporter and reverse transcription polymerase chain reaction (RT-PCR) of *PIN1* in seedlings (Fig. 1A) and cultured cells (fig. S2). In estradiol-treated *XVE-PIN1* cells, the overexpressed PIN1 was localized at the PM (Fig. 1, B and C). The syn-